Available online at www.sciencedirect.com
ScienceDirect
Journal of Non-Crystalline Solids 352 (2006) 5353–5361
JOURNAL OF NON-CRYSTALLINE SOLIDS
www.elsevier.com/locate/jnoncrysol

Color variations in 13th century hispanic lustre – An EXAFS study

A.D. Smith [a,*], T. Pradell [b], J. Roqué [c], J. Molera [d], M. Vendrell-Saz [c], A.J. Dent [e], E. Pantos [a]

[a] Synchrotron Radiation Department, CCLRC Daresbury Laboratory, Keckwick Lane, Daresbury, Warrington, Cheshire WA4 4AD, United Kingdom
[b] Departament Fisica i Enginyeria Nuclear ESAB-UPC Campus Baix Llobregat, Av. Canal Olímpic, 08860 Castelldefels, Barcelona, Spain
[c] Departament de Cristallografia i Mineralogia Universitat de Barcelona, 08028 Barcelona, Spain
[d] Departament de Física, Universitat de Girona, 17071 Girona, Spain
[e] Diamond Light Source Ltd. Chilton, Didcot, Oxfordshire, OX11 0DE, United Kingdom

Received 6 February 2006; received in revised form 2 August 2006

Abstract

Microprobe EXAFS analysis of lustre decoration from a late 13th century Hispano–Moresque potsherd has been used to examine the metallic oxide to metal ratios in different shaded copper lustre finishes. A single specimen from 13th century Paterna, exhibiting typical red and green colorations, is found to contain different copper/silver ratios depending on the color. EXAFS has been used to determine the local atomic environment of the copper and reveals a corresponding variation in the metal to oxide ratio of the copper content which is related to the visual effect.

PACS: 61.10.Ht; 61.46.+w; 81.05.Je

Keywords: Oxidation reduction; Archaeology; X-ray fluorescence; Short range order; X-ray absorption

1. Introduction

Lustre is a metallic decoration applied to ceramics and dates from the early 9th century islamic period through to medieval and renaissance western Mediterranean. It is formed by applying a copper and silver based paint to an already glazed and fired pot. The ceramic then undergoes another firing, this time in a reducing atmosphere, during which time copper and silver ions are drawn into the glaze via an ionic exchange mechanism [1]. The metal ions are reduced and aggregate together to form nanoclusters [2–7]. Lustre finishes exhibit a wide range of colors, depending upon their chemical composition, from yellow, green and browns for silver rich lustres to orange, reds and crimsons for copper rich lustres [8,9].

Paterna was a major production center of lustreware in the late 13th through to the 15th centuries. In common with many other lustres, these show two main colors, red for thin line drawings and edges of thicker lines or motifs, and green for the thicker lines or large motifs. We selected a single specimen, shown in Fig. 1, from the 13th century workshop exhibiting the two major colors commonly seen. The main body of the decoration (circular area in the upper half of Fig. 1) is greenish[1] in color, whilst the finer lines that cross this are more red. Closer investigation shows that the edge of the green decoration is in fact red. As these changes in color occur in the same decoration, it can be expected that they were applied at the same time, using the same raw material and fired simultaneously.

A number of complementary techniques have been used in the past to characterize lustre and to understand the

* Corresponding author. Tel.: +44 1925603314; fax: +44 1925603124.
E-mail address: a.d.smith@dl.ac.uk (A.D. Smith).

[1] For interpretation of color in Figs 1–3, the reader is referred to the web version of this article.

0022-3093/$ - see front matter © 2006 Elsevier B.V. All rights reserved.
doi:10.1016/j.jnoncrysol.2006.08.024

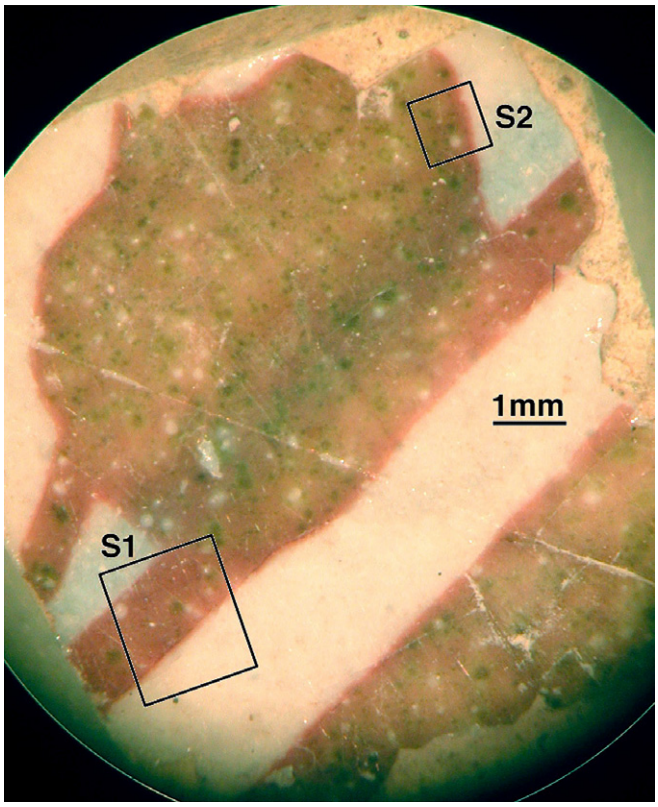

Fig. 1. Light microscope image of M11 pot sherd, showing two regions selected for data analysis. Lower left (S1) on red band (see Fig. 2) and upper right (S2) on green decoration (see Fig. 3). The scale bar is 1 mm. The blue–grey band running from lower right to upper left is a different type of decoration, found by XRF to be zinc based.

lustre making process, these have included electron microscopy to image the nanoparticles and directly measure their size [2–4,6] extending to energy dispersive X-ray analysis (SEM-EDX) [1,3,4,6,8,10,11] to determine the chemical composition and elemental distributions. Atomic force microscopy (AFM) has additionally been utilized [7] to measure the effect on surface roughness due to the growth of nanoparticles below the glaze surface. To identify the crystalline phases present and their size, X-ray diffraction has been employed [11,12]. UV–visible absorption spectroscopy is useful for giving a direct measure of the color of the lustre, rather than having to rely on a visual interpretation of that color. Moreover, the presence of surface plasmon resonances (SPR) in the absorption are characteristic of copper and silver nanoparticles, these affect the final color show by the lustre layer. The SPR peak wavelength being shifted by an amount dependant upon the nanoparticle size and the composition of the glaze [2,3,8,11] so giving indirect information on the type and size of the metal nanoparticles present. Luminescence resulting from photon stimulated emission, using visible laser, UV or X-rays can indicate the presence of Cu^{+} and Ag^{+} ions in the glaze [13].

EXAFS (Extended X-ray Absorption Fine Structure [14]) has been used [1,5,15–17] to provide detailed information on the local atomic configuration of the copper and identify the existence of copper in a metallic or oxidized form. As EXAFS probes the environment around individual atoms, it can determine quantitative information on the chemical bonds over very short range scales and does not need a high degree of crystallinity in the sample.

In this study, we have used microbeam EXAFS to probe the variation in copper chemistry corresponding to the color variations seen in this sample. By choosing this technique, we have been able to explore the chemical variations in the lustre on a small spatial scale and resolve differences not only between different decorations on a single potsherd sample, but also within a single decoration and be able to correlate this chemical difference with the visual effect seen.

2. Experimental

Data was collected on the microEXAFS beamline, 10.3.2, at the ALS [18]. Two modes of data collection are available: firstly, elemental imaging of the X-ray fluorescence (XRF) using an energy resolving Si(Li) detector to simultaneously record concentrations of a variety of elements by measuring the intensity of various fluorescence emission lines; secondly, Cu K-edge EXAFS measurements can also be taken at particular positions on the sample. Spatial resolution of the focal spot is approximately 20 μm × 5 μm, with the option of reducing this further but at the expense of flux. Elemental maps, such as those

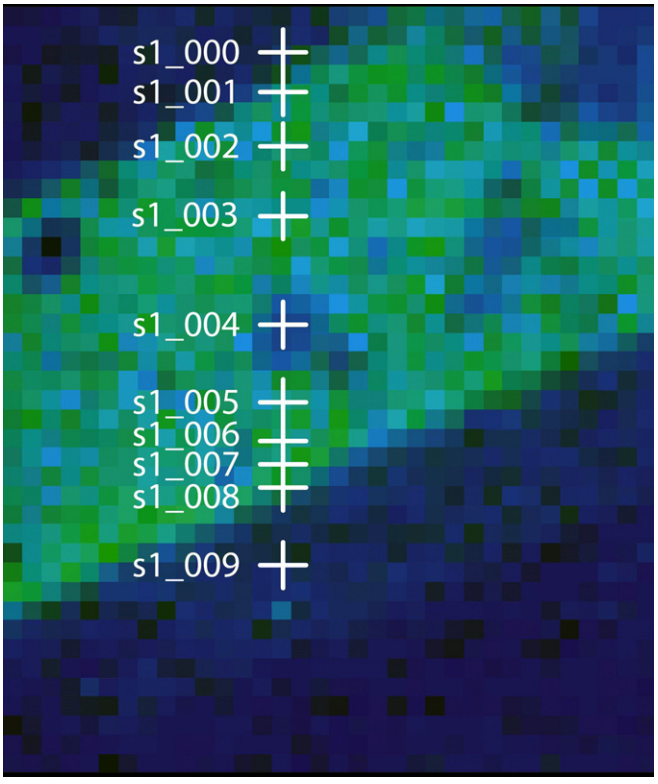

Fig. 2. Color composite of 1.7 mm × 2 mm region over red band from which S1 transect was taken. Pixel size is 50 μm. Green corresponds to copper content, blue to silver.

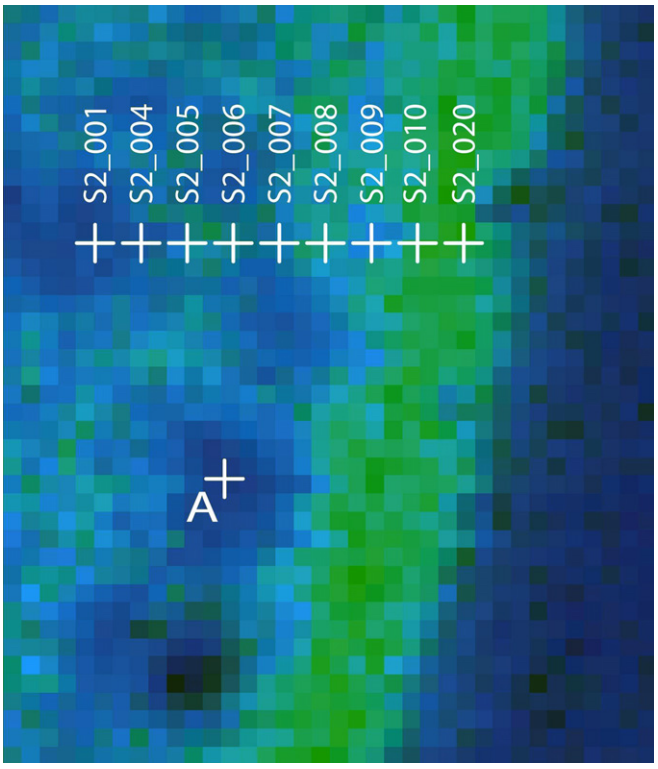

Fig. 3. Color composite of green region from which S2 transect was taken. Area = 0.85 mm × 0.83 mm, pixel size is 20 μm. Green corresponds to copper content, blue to silver. Location marked A is a high silver region from which a separate Ag L-edge EXAFS analysis, shown in Fig. 7, was taken.

shown in Figs. 2 and 3, have a pixel size that is determined by the step size used in raster scanning the sample. This step size is user definable and generally adjusted to compromise between detail and time taken to record an image. The instrument has not been calibrated to provide absolute elemental concentrations by XRF, however a figure for typical values in the two colors comes from independent measurements in an EPMA Cameca SX-50 microprobe. Data from multichannel analysis (MCA) of the detector output, however, provides relative elemental concentrations and can be precisely correlated to the EXAFS analysis, being collected from the same sample locations whilst in the same instrument. EXAFS provides local atomic ordering and hence chemical speciation.

The order of measurements was to first collect a raster scan of the sample using the micro focussed beam at a monochromatic energy of 11 keV. This enables a series of elemental maps to be constructed confirming registration of sample position and highlighting particular areas of interest. Two sampling lines or transects were subsequently defined crossing the red band (S1 series of data points) and through the edge of the green main feature (S2 series). For each point in the transect both a MCA scan and a Cu K-edge EXAFS spectrum were acquired.

Intensities for the fluorescence emission lines were calculated by curve fitting gaussian profiles to the copper and silver lines in the MCA spectra. The silver emission is only partially resolved from the K and Ca fluorescence lines, in this instance a triple gaussian was fitted to all three lines with the width predetermined from the detector response at the copper Kα emission line. The energy resolution of the detector was found to be 290 eV FWHM. The gaussian fitting process gives a peak intensity with an associated error based on all the collected events from that fluorescence line, rather than just using the value in the MCA channel corresponding to the peak. The error in determining the peak intensity is therefore reduced. For the Ag intensity, this is deconvolved from the influences of the neighboring, and overlapping, K and Ca responses. At the softer X-ray energy of these latter absorption lines, the signal intensity is reduced, partly due to a lower fluorescent yield, but principally due to increased absorption of the softer energy fluorescence X-rays by the air path between sample and detector, and by the detector window itself.

EXAFS data for each selected point came from a single scan and was deadtime corrected to remove detector non-linearities. Background subtraction was conducted using EXSPLINE [19] and analysis performed with EXCURV98 [20]. As previous evidence indicates a mixture of metal and oxide copper forms [5,16], a two cluster model starting with copper metal and cuprite (Cu_2O) was adopted. Due the expected enhancement of the 4th metal shell (5.113 Å) from multiple scattering off the first metal shell (2.556 Å), the multiple scattering option was selected. Refinement was limited to the Debye–Waller factors (A_n), shell radii (R_n), Fermi energy (E_f) and the metal/oxide ratio, $N0$. With the exception of the oxide Cu–Cu shell, the model refined these within sensible limits without the need to adjust the coordination numbers (N_n). The Cu–Cu shell for the cuprite component was less easy to fit and appeared poorly defined in the experimental data, yielding relatively high Debye–Waller factors and/or significantly reduced coordination numbers. The Debye–Waller factor is a measure of the atomic disorder in the system, both thermal and static. EXCURV98 uses Debye–Waller factors equivalent to $2\sigma^2$ and in units of $Å^2$, σ being mean square variation in atomic separation.

3. Results

Fig. 2 shows an elemental map of a 1.7 mm × 2 mm area of the sample, covering the part of the red band shown by the lower left box on Fig. 1. Green represents the copper content with silver and potassium in blue. Limited resolution of the Si(Li) detector restricts clear separation of the Ag and K content in this mode. It is clear that the copper concentration is fairly uniform throughout the width of the decoration, with only a few missing patches, due either to missing lustre (such as upper left) or coinciding with an increased silver content and a localized green color in the lustre. This is highlighted at the point marked s1_004 and in the upper right corner, this latter area is part of the larger green decoration. Independent measurements

in the Cameca give a copper content of approximately 1.2 ± 0.1 wt% throughout this band, dropping to 0.4 ± 0.4 wt% in the silver rich spot. The silver content is about 0.4 ± 0.2 wt% in the main part of the decoration, rising to 4.8 ± 2.5 wt% in the silver concentrated spot. This is typical of the silver distribution observed in lustres, where high silver content particles congregate in small localized areas, leading to a very inhomogeneous silver distribution.

Fig. 3 is a similar map of a 0.85 mm × 0.83 mm area at the edge of the main decoration, highlighted by the upper-right box in Fig. 1. This shows that the main part of the decoration is relatively low in copper and with an increased quantity of silver, except at the very edge where the copper concentration is higher. This corresponds to the red edge that is seen at this point. It is apparent that except at its very outer edge, the quantity of copper in the green decoration is lower than in the red decoration. A simultaneously collected silver map indicates that the silver is inversely correlated with the copper and has a higher concentration in the green decoration. Measurements from the Cameca give a silver content of 3.0 ± 0.8 wt% and 0.2 ± 0.1 wt% copper in the main body of this decoration. At the very edge the silver concentration drops to less than 0.4 wt% whilst the copper rises to 0.6 wt%.

These two areas are used as basis for defining sampling transects, S1 and S2, measuring across a thin red line, and across a green decoration simultaneously. EXAFS analyzes were performed at each of the points marked on Figs. 2 and 3.

The EXAFS data are shown in Figs. 4 and 5 for the two transects. The (a) parts of the figures show the background subtracted and k^2 weighted k-space data, the (b) parts show the corresponding Fourier transformed data. For all data sets the experimental data (solid lines) and the theoretically modelled fitted data (dashed lines) are shown. The fourier transformed data show two principle shells, a Cu–Cu bond at approximately 2.56 Å and a Cu–O bond at about 1.85 Å. The former corresponds to the first shell in copper metal, the latter to the first shell in cuprite. It should be noted that attempts to encourage the refinement to adopt a Cu–O bond distance of 1.96 Å, the distance for tenorite, failed with the model consistently refining to the cuprite bond length. This suggests that the oxide present is a partially reduced form. Large errors, high Debye–Waller factors and reduced coordination numbers were obtained for the cuprite Cu–Cu shell. This implies a high degree of disorder in the oxide and a lack of any long range order. Electron diffraction measurements [17] on other lustre samples have revealed nanoparticles comprising of copper metal, but not oxide. This suggests that the oxide is due to isolated copper atoms in the glassy matrix which are still undergoing reduction, hence are in a partially reduced form, and which have yet to form into clusters. EXAFS is sensitive to short range atomic order, so can identify the oxide phase within a largely amorphous structure.

A summary of the EXAFS results for the primary metal and oxide shells is given in Table 1. Additionally the fraction of metal to oxide is also given, this can be seen to vary between 0.1 and 0.7, with the lower fractions corresponding to a reduced overall copper content. This also gives a lower signal to noise level in the EXAFS data and hence larger errors in the analysis. For comparison, data of three

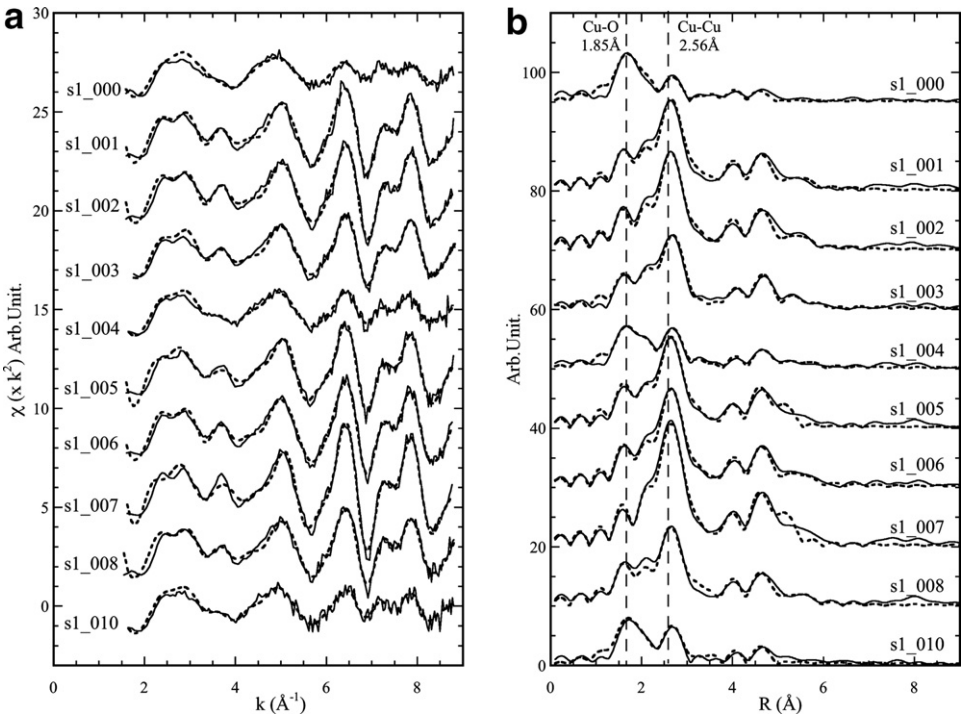

Fig. 4. EXAFS data extracted from along the S1 transect of the red band. (a) Is the background subtracted and k^2 weighted k-space data, (b) is the corresponding Fourier transforms. Solid lines are experimental data, dashed lines are the modelled fit. R is distance from central atom.

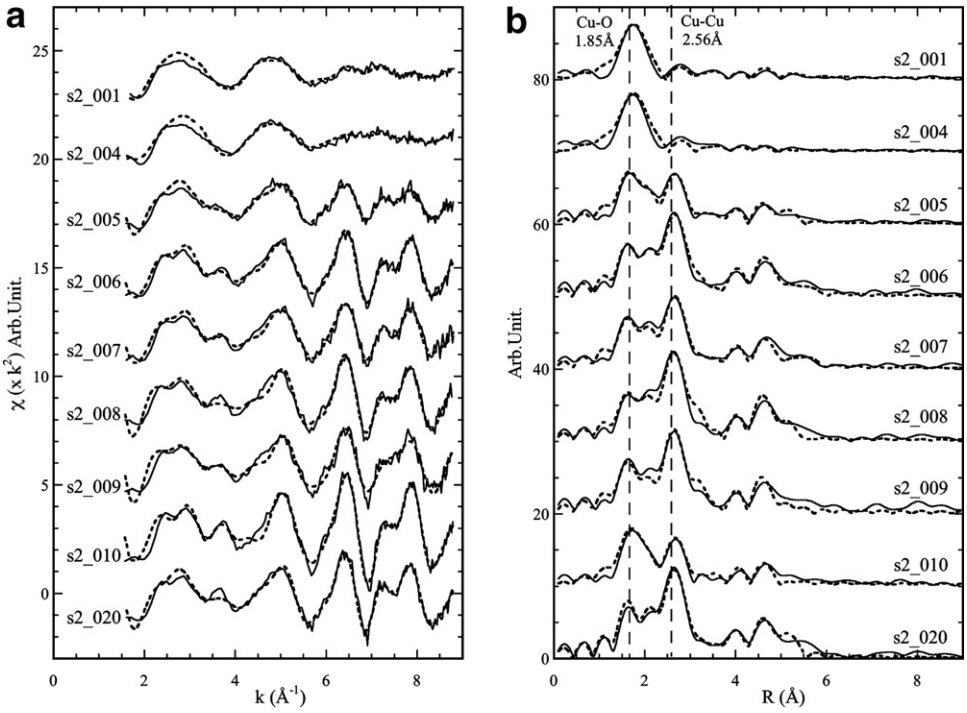

Fig. 5. EXAFS data extracted from along the S2 transect of the green decoration. (a) Is the background subtracted and k^2 weighted k-space data, (b) is the corresponding fourier transforms. Solid lines are experimental data, dashed lines are the modelled fit. R is distance from central atom.

Table 1
EXAFS analysis across the two transects, including model data and analysis of model compounds

	EXAFS fit to first shells								
	Shell 1: Cu–Cu (Metal)			Shell 2: Cu–O (oxide)					
	N	R (Å)	A (Å^2)	N	R (Å)	A (Å^2)	$N0$	Fit index	Chi-sq
S1_000	12	2.57 ± 0.02	0.025	2	1.86 ± 0.02	0.016	0.2 ± 0.1	40.48	9.07
S1_001	12	2.55 ± 0.01	0.018	2	1.84 ± 0.03	0.004	0.6 ± 0.1	21.22	2.76
S1_002	12	2.55 ± 0.01	0.015	2	1.83 ± 0.04	0.014	0.6 ± 0.1	19.56	2.29
S1_003	12	2.55 ± 0.01	0.018	2	1.85 ± 0.03	0.019	0.5 ± 0.1	21.10	2.58
S1_004	12	2.57 ± 0.02	0.021	2	1.86 ± 0.02	0.015	0.3 ± 0.1	33.06	6.71
S1_005	12	2.55 ± 0.01	0.016	2	1.85 ± 0.03	0.005	0.6 ± 0.1	23.43	3.32
S1_006	12	2.55 ± 0.01	0.017	2	1.85 ± 0.03	0.001	0.7 ± 0.1	20.00	2.11
S1_007	12	2.55 ± 0.01	0.013	2	1.85 ± 0.05	0.009	0.7 ± 0.1	19.00	2.14
S1_008	12	2.55 ± 0.01	0.018	2	1.85 ± 0.04	0.010	0.5 ± 0.1	24.78	4.09
S1_010	12	2.58 ± 0.02	0.028	2	1.87 ± 0.03	0.011	0.4 ± 0.1	42.89	10.35
S2_001	12	2.61 ± 0.03	0.036	2	1.88 ± 0.02	0.016	0.1 ± 0.1	41.26	10.44
S2_004	12	2.60 ± 0.03	0.020	2	1.87 ± 0.01	0.020	0.1 ± 0.1	42.91	11.49
S2_005	12	2.56 ± 0.01	0.024	2	1.86 ± 0.02	0.015	0.4 ± 0.1	34.82	6.84
S2_006	12	2.56 ± 0.01	0.017	2	1.85 ± 0.03	0.016	0.4 ± 0.1	21.47	2.81
S2_007	12	2.55 ± 0.01	0.020	2	1.85 ± 0.03	0.019	0.4 ± 0.1	29.37	4.96
S2_008	12	2.55 ± 0.01	0.018	2	1.88 ± 0.03	0.013	0.5 ± 0.1	27.93	4.54
S2_009	12	2.56 ± 0.01	0.021	2	1.84 ± 0.04	0.010	0.5 ± 0.1	33.57	7.05
S2_010	12	2.54 ± 0.01	0.017	2	1.82 ± 0.06	0.019	0.7 ± 0.1	21.10	3.08
S2_020	12	2.56 ± 0.01	0.014	2	1.86 ± 0.02	0.009	0.5 ± 0.1	23.28	3.42
Mean	12	2.55 ± 0.01	0.020 ± 0.006	2	1.86 ± 0.01	0.012 ± 0.006			
Theory	12	2.556		2	1.85				

N is the shell occupancy, R is the shell distance from the central atom and A the Debye–Waller factor. $N0$ is the ratio of metal to oxide component as calculated from the EXAFS. The fit index and Chi-squared values are discussed in the text.

model compounds (copper metal, cuprite and tenorite) collected at the Daresbury SRS were also analyzed to confirm the expected differences between the three copper species. The results are shown in Fig. 6 and tabulated in Table 2. The Cu–Cu shells at 2.556 Å, 4.428 Å and 5.113 Å in copper metal give a strong response, which can be seen throughout the spectra obtained from the lustre sample and are also evident in Figs. 4 and 5. The shift in the

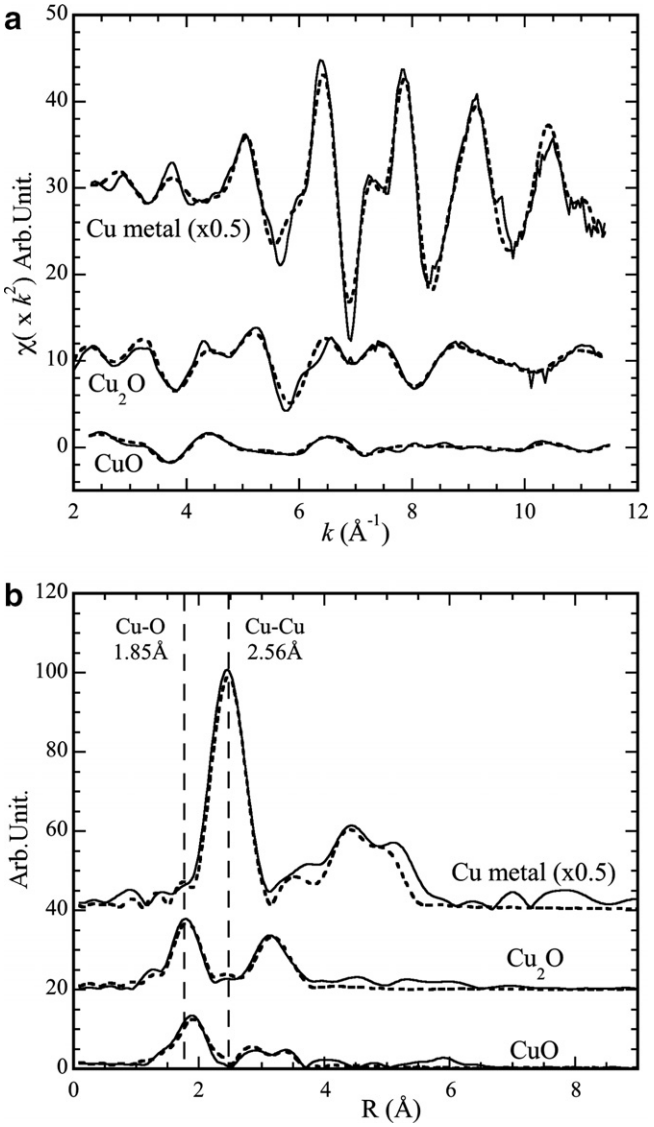

Fig. 6. EXAFS data of 3 model compounds, copper metal, cuprite (Cu_2O) and tenorite (CuO). Solid lines are experimental data, dashed lines are modelled fit. (a) Shows the k^2 weighted k-space data with (b) being the corresponding fourier transformed data. R is distance from central atom.

Cu–O bond length between cuprite (1.85 Å) and tenorite (1.96 Å) is also distinct.

The EXAFS analysis indicates that in all locations, a combination of metallic and oxide copper contributions is needed. The first Cu–Cu shell distance is found to have a range from 2.542 Å to 2.611 Å with a mean across all measurements of 2.552 ± 0.002 Å, in agreement with the theoretical value of 2.556 Å. The second and third Cu–Cu shells of 6 copper atoms at 3.606 ± 0.006 Å and 24 copper atoms at 4.468 ± 0.004 Å respectively, are also in good agreement with theoretical values of 3.615 Å and 4.428 Å. A full fourth shell of 12 copper atoms at 5.199 ± 0.005 Å is also found (theoretical values of 5.113 Å), although the quality of fitting this is directly related to the data quality, corresponding with Debye–Waller factors of much greater variability (typically

Table 2
EXAFS analysis of model compounds

	$N1$	$R1$ (Å)	$A1$ (Å^2)	$N2$	$R2$ (Å)	$A2$ (Å^2)	$N3$	$R3$ (Å)	$A3$ (Å^2)	$N4$	$R4$ (Å)	$A4$ (Å^2)	Fit index	Chi-sq
Cu metal	Shell 1: Cu–Cu			Shell 2: Cu–Cu			Shell 3: Cu–Cu			Shell 4: Cu–Cu				
Experiment	12	2.55 ± 0.01	0.016	6	3.60 ± 0.02	0.022	24	4.45 ± 0.01	0.019	12	4.94 ± 0.01	0.008	25.23	2.07
Theory	12	2.556		6	3.615		24	4.428		12	5.113			
Tenorite (CuO)	Shell 1: Cu–O			Shell 2: Cu–O			Shell 3: Cu–Cu			Shell 4: Cu–Cu				
Experiment	4	1.97 ± 0.01	0.013	2	2.49 ± 0.07	0.065	4	2.89 ± 0.01	0.013	4	3.07 ± 0.01	0.016	26.43	1.91
Theory	4	1.955		2	2.78		4	2.90		4	3.08			
Cuprite (Cu2O)	Shell 1: Cu–O			Shell 2: Cu–Cu										
Experiment	2	1.86 ± 0.01	0.016	12	3.03 ± 0.01	0.051							45.72	7.12
Theory	2	1.85		12	3.02									

The Nn, Rn and An values have the same meanings as N, R and A in Table 1, but relate to the nth shell.

0.017 Å^2, but as high as 0.093 Å^2) than found for the other shells (average of 0.020 Å^2, maximum of 0.039 Å^2 for the three inner shells). A full outer shell indicates that the cluster size is considerable and probably in excess of 2000 atoms [21]. Considering the molar volume of copper metal (7 cm^3) this implies a particle size greater than 3 nm. Lustres typically exhibit particle sizes in the range 5–20 nm or larger [3,4,6], so a reduction in shell occupancy would not be expected to be detected using EXAFS. The errors quoted for the weighted averages do mean that some of the values obtained fall a little outside of the expected values, which implies an underestimation of the errors in the analysis.

EXCURV98 uses the reduced χ^2 function [22] to give an absolute index of goodness of fit which takes account of the degree of over determinacy in the system. A second measure of the goodness of fit of the model to the EXAFS data is provided by the *R* factor, this is a least squared deviation of theory from experimental data in *k*-space. A value of 20% is generally considered to be a good fit to the data, As can be seen from Table 1 most of our measurements lie in the 20–30% range, the exceptions being for those locations with low fractions of copper metal (low values of *N*0). These were also the places with least copper present, so providing the least signal. Correspondingly the signal to noise ratio was degraded giving poorer quality data and hence a higher fit-index. Inspection of the *k*-space data in Figs. 4 and 5 do show spectra which look more oxide like at these places.

A silver L-edge EXAFS spectrum was also collected from the silver rich area indicated by 'A' in Fig. 3. The close proximity of the Ag L_2 line to the L_3 line limits the L-edge spectral range to about $k = 7$, which is generally considered too short to provide much useful EXAFS information. However, the relatively heavy scattering of the silver atoms provides a strong oscillation and we obtained sufficient information to provide a reasonable fit to silver metal. The results are shown in Fig. 7 and agree well with those expected for silver metal. Silver metal has the same fcc crystal structure as copper metal, although with a larger *d*-spacing. so the corresponding bond lengths for the first four shells are 2.892 Å, 4.090 Å, 5.009 Å and 5.785 Å.

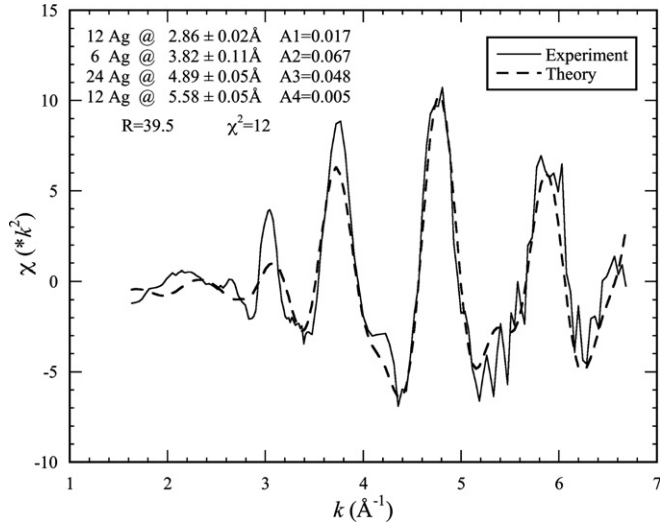

Fig. 7. Ag L-edge EXAFS from the silver rich area ('A' in Fig. 3) in the green decoration. The fit parameters are summarized in upper left, number of Ag atoms in each shell, shell radius given in Angstrom with the Debye–Waller factor (*A*) in Å^2. *R* is the fit index expressed as a percentage, the reduced χ^2 function is also given.

4. Discussion

Figs. 8 and 9 show the metal/oxide fraction along with the copper and silver content for the two transects. These show a distinct correlation between the three factors. Firstly there is an inverse correlation between silver and copper content. This is particularly pronounced in the silver rich spot seen in the S1 transect at s1_004, but also shows some evidence crossing the S2 transect. Secondly, there is a distinct correlation between copper content and fraction of copper metal. In other words, as the copper content increases, the copper is more likely to be metallic in nature with a smaller fraction still in oxide form. The red decoration appears to have a higher elemental copper concentration than the green areas. These red regions also have a higher percentage of copper metal, as opposed to oxide, present. It is noted that the red coloration is most evident on the edges of decorations, or throughout the width of finer decorations.

As the color variation can be observed in the same decoration, as in the case of the red rim to the larger green decoration, it is expected that both the original material and the production process (firing conditions) are the same

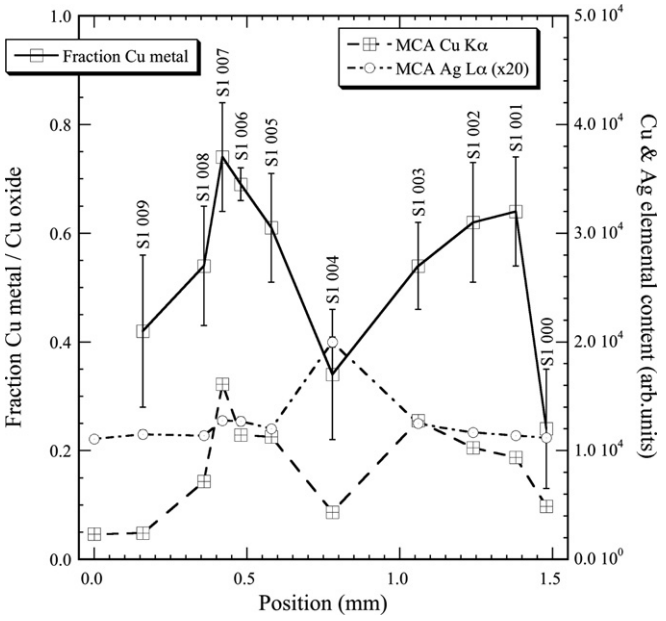

Fig. 8. Summary of MCA and EXAFS information along transect S1 over the red band. The metal/oxide ratio is provided by the parameter *N*0 from the EXAFS analysis. The abscissa refers to the distance along the transect.

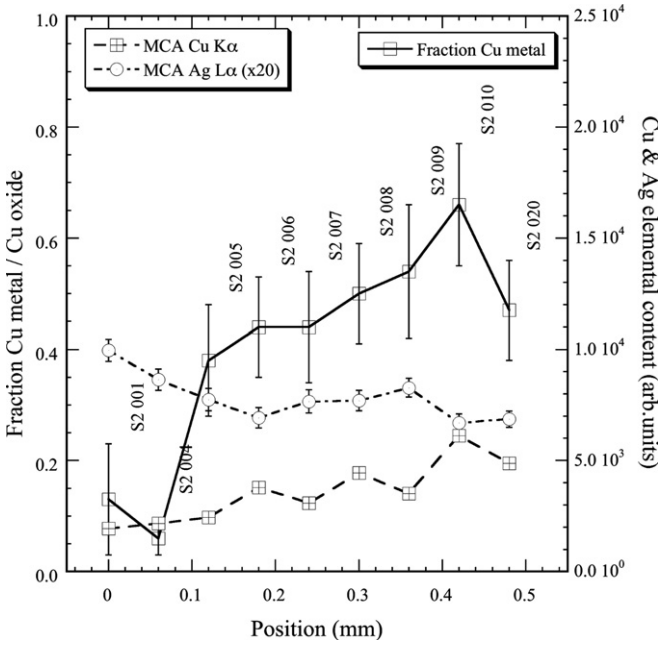

Fig. 9. Summary of MCA and EXAFS information across transect S2 over the green band. The metal/oxide ratio is provided by the parameter *N*0 from the EXAFS analysis. The abscissa refers to the distance along the transect.

for both colors. Reproduction of lustre under laboratory conditions has provided an insight into the lustre forming process [11,23]. Using a recreation of the 13th century Paterna recipe [9], the onset of lustre creation is driven by ionic exchange between alkali ions in the glaze (Na^+ and K^+) with the metal ions (Cu^+ and Ag^+) from the paint. Moreover, Cu^+ is ion exchanged under oxidising conditions, whereas Ag^+ requires reducing conditions for exchange. Reducing conditions are subsequently required by both metals for reduction to Cu^0 and Ag^0 states and the formation of metal nanoparticles within the glaze.

The lustre firing is done in a reducing atmosphere, in the traditional kiln by burning rosemary wood. However in such a kiln there is a necessary earlier stage of wood burning to get the kiln and its contents to an operating temperature. This requires an oxidising atmosphere and is responsible for the initial ion-exchange mechanism that enables copper take up by the glaze. This process takes place at the interface between the glaze and the lustre paint, however, the paint itself forms a semi-protective coating on the glaze which can restrict the diffusion of the kiln atmosphere to the glaze surface. At the edges of the applied paint, there is a second conductive path open to the atmosphere, along the boundary itself. Thus it is expected that there will be an initial take up of copper by the glaze along the edges of the decorations. For small decorations this edge preference could penetrate throughout the applied pattern, turning the whole decoration a deeper, redder and more coppery color.

Once the kiln reaches its required temperature of about 500 °C, the atmosphere becomes reducing. Under such conditions, silver is more easily ion exchanged than copper. It also reduces more quickly than copper does, so the process now favours Ag uptake and reduction. The copper already ion exchanged in the glaze also undergoes reduction and nanoparticle formation, but is limited by the quantity of copper already in the glaze. The center of the large decorations, therefore, has a higher silver to copper ratio than the edges. We suspect that the ease with which silver can be reduced restricts its mobility within the glaze, leading to the formation of high silver content areas, such as the feature observed at location S1_004 in Fig. 2. Similar spots and inhomgeneities are often observed in silver rich lustre finishes from both antiquity and modern times.

The differences between red and gold decorations, and the corresponding differences in copper metal/oxide ratios have been determined before using EXAFS [5,13]. However, the earlier studies probed different decorations on separate potsherd samples, here, we have used MicroEXAFS analyzes to probe variations between decorations on a single sample and variations within the individual patterns. We have therefore been able to demonstrate that the different color effects do not arise from variations in either the raw material applied, or in the process technology used, but from variations within that process itself.

The variation in finish color between small and large decorations, and between the center and edge of the latter will have surely been noted by the observant potter, even if he was unable to explain why. Using XRF mapping and EXAFS, we have demonstrated that throughout a small decoration and at the edge of a larger decoration in a 13th century potsherd that there is a higher copper content with a higher proportion of the copper in a metallic phase, than in the center of a larger decoration. This latter is more silver rich. These differences correlate with the visual effect. The skilled artisan will have had little scope for altering these effects, but will have undoubtedly tried to incorporate them in his designs.

Acknowledgments

Reference EXAFS spectra of the copper oxides, cuprite and tenorite, were kindly provided by Dr John Charnock of the University of Manchester. We also wish to thank Dr Matthew Marcus of the Advanced Light Source (ALS) for help in setting up the experiments. The ALS is supported by the Director, Office of Science, Office of Basic Energy Sciences, of the US Department of Energy under Contract No. DE-AC02-05CH11231. T. Pradell acknowledges the financial support from CYCIT, Grant MAT2004-01214.

References

[1] T. Pradell, J. Molera, J. Roqué, M. Vendrell-Saz, A.D. Smith, E. Pantos, D. Crespo, J. Am. Ceram. Soc. 88 (2005) 1281.
[2] J. Pérez-Arantegui, J. Molera, A. Larrea, T. Pradell, M. Vendrell-Saz, I. Borgia, B.G. Brunetti, F. Cariati, P. Fermo, M. Mellini, A. Sgamellotti, C. Viti, J. Am. Ceram. Soc. 84 (2001) 442.
[3] G. Padeletti, P. Fermo, Appl. Phys. A 76 (2003) 515.

[4] J. Pérez-Arantegui, A. Larrea, J. Molera, T. Pradell, M. Vendrell-Saz, Appl. Phys. A 79 (2004) 235.
[5] S. Padovani, I. Borgia, B. Brunetti, A. Sganellotti, A. Giulivi, F. D'Acapito, P. Mazzoldi, C. Sada, G. Battaglin, Appl. Phys. A 79 (2004) 229.
[6] P. Fredrickx, D. Hélary, D. Schryvers, E. Darque-Ceretti, Appl. Phys. A 79 (2004) 283.
[7] J. Roqué, T. Pradell, J. Molera, M. Vendrell-Saz, J. Non-Cryst. Solids 351 (2005) 568.
[8] I. Borgia, B. Brunetti, A. Giulivi, A. Sgamellotti, F. Shokouhi, P. Oliaiy, J. Rahighi, M. Lamehi-Rachti, M. Mellini, C. Viti, Appl. Phys. A 79 (2004).
[9] J. Molera, M. Mesquida, J. Pérez-Arantegui, T. Pradell, M. Vendrell, Archaeometry 43 (2001) 455.
[10] A. Romani, C. Miliani, A. Morresi, N. Forini, G. Favaro, Appl. Surf. Sci. 157 (2000).
[11] T. Pradell, J. Molera, C. Bayés, P. Roura, Appl. Phys. A 83 (2006) 203.
[12] G. Padeletti, P. Fermo, Appl. Phys. A 79 (2004) 241.
[13] S.E. Paje, J. Llopis, M.A. Villegas, J.M. Fernández Navarro, Appl. Phys. A 63 (1996) 431.
[14] S.J. Gurman, J. Synchrotron Radiat. 2 (1995) 5.
[15] S. Padovani, C. Sada, P. Mazzoldi, B. Brunetti, I. Borgia, A. Sgamellotti, A. Giulivi, F. D'Acapito, G. Battaglin, J. Appl. Phys. 93 (2003) 10058.
[16] A.D. Smith, T. Pradell, J. Molera, M. Vendrell-Saz, M.A. Marcus, E. Pantos, J. de Phys. IV 104 (2003) 519.
[17] J. Roqué, N.R.J. Poolton, J. Molera, A.D. Smith, E. Pantos, M. Vendrell-Saz, Phys. Stat. Sol. (b) 243 (2006) 1337.
[18] M.A. Marcus, A.A. McDowell, R. Celestre, A. Manceau, T. Miller, H.A. Padmore, R.E. Sublett, J. Synchrotron Radiat. 11 (2004) 239.
[19] EXSPLINE : Daresbury Laboratory, 2000. Based on an original program, SPLINE, P.Ellis, PhD thesis, University of Sydney, 1998.
[20] N.Binsted, EXCURV98: CCLRC Daresbury Laboratory computer program, 1998.
[21] A. Jentys, Phys. Chem. Chem. Phys. 1 (1999) 4059.
[22] F.W. Lytle, D.E. Sayers, E.A. Stern, Physica B 158 (1989) 701.
[23] J. Molera, C. Bayés, P. Roura, D. Crespo, T. Pradell, J. Amer. Ceram. Soc., under revision.